Seismic Performance of High-Strength Steel Fiber Reinforced Concrete Column under Bidirectional Bending and Varying Axial Loading

Satoshi Kake*1 Fumitaka Ogura*2 Naoki Aso*3
Yoshihiro Ohta*4 Hideki Kimura*5 Yuji Ishikawa*6

Summary

This paper reports on the seismic performance of a high-strength steel fiber reinforced concrete (SFRC) column under varying axial loading and a clover-shaped lateral loading. The SFRC column specimen did not experience spalling of cover concrete until the deformation angle R=30×10^{-3} rad due to the good effect of steel fibers. Furthermore, by the influence of the kinematic hardening of the yield surface, the maximum strength of the specimen was recorded at a loading angle of about θ=31° where the X or Y-directional deformation began to decrease. Also, the ultimate flexural strength of the specimen was appropriately estimated by using the ACI formula based on the stress block, and Ferguson's proposal.

Keywords: high-strength RC column, steel fiber reinforced concrete, bidirectional bending, ultimate flexural strength, kinematic hardening

1 Introduction

Various studies on high-strength concrete with a compressive strength of f'_c=100N/mm^2 class were carried out in the New RC project[1] in the 1980s with the aim of realizing a high-rise reinforced concrete (RC) building. In recent years, research and development[2] of ultra-high-strength concrete with compressive strength exceeding f'_c=150N/mm^2 has been carried out, and in some cases, it has been adopted for columns with high axial forces, such as those in the lower floors of super high-rise RC buildings[3].

High-strength concrete has high compressive strengths and can resist higher stresses than normal concrete, however, when stresses in the concrete reach the compressive strength, the stored energy is rapidly released, causing a brittle crushing failure. Research[2] on high strength RC columns has shown that failure of cover concrete was more brittle when such RC columns with a high axial loading ratio reached their ultimate flexural strengths, and that spalling occurred over a wide area.

In order to improve the structural performance of high-strength RC columns by preventing the crush of cover concrete, structural tests[4)~6)] of SFRC columns using steel fiber reinforced concrete were carried out under static loading in one direction. As shown in Photo 1, as steel fibers, which are dispersed in the concrete of the SFRC columns, resist the tensile forces acting on the member, they can minimize the damage on cover concrete during earthquakes. In addition, it has been reported that the reduction in flexural strength of SFRC columns due to damage to the cover concrete is more gradual than that of RC columns with plain concrete[5),6)].

As actual structures are subjected to seismic forces in multiple directions rather than in one direction and corner columns in the lower stories of high-rise RC buildings in particular undergo varying axial loads accompanied by bending moments, cover concrete of some columns may experience more severe stress conditions compared to that of corner columns under unidirectional lateral loads. However, there are very few research studies on high-strength SFRC columns subjected to multidirectional lateral loads.

Meanwhile, research on elements of RC structures under multidirectional loads has been conducted based on bending theory[7] since the 1960s using the fiber model for elements' sections. Many experiments have primarily focused on RC columns below f'_c=60N/mm^2. They included some studies where, to simulate multidirectional bending, columns' cross-section directions were horizontally rotated, and consequently, only a unidirectional lateral loading was applied[8] (Fig. 1 (a)), and some other studies

*1 Researcher, Structural Engineering Dept., Research & Development Institute
*2 Building Design Department, Tokyo Main Office
*3 Engineering Department
*4 General Manager, Structural Engineering Dept., Research & Development Institute, Dr.Eng.
*5 Executive Manager, Research & Development Institute, Dr.Eng.
*6 Professor, College of Systems Engineering and Science, Shibaura Institute of Technology, Dr.Eng.

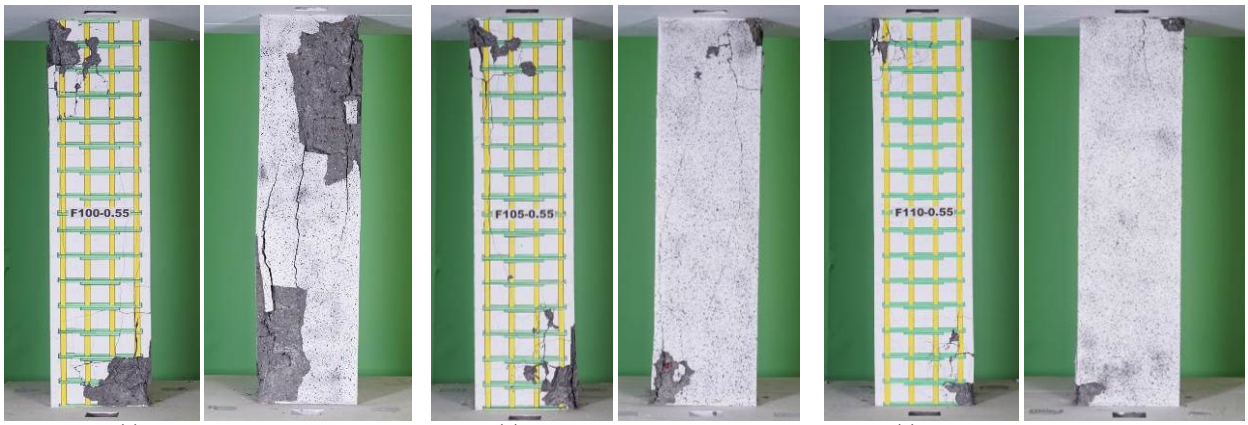

(a) No steel fiber (b) Steel fiber：0.5 Vol.% (c) Steel fiber：1.0 Vol.%

Photo 1 Damage of high strength reinforced concrete column after the test[6] (After R=30×10^{-3} rad)

where column head displacements were laterally loaded in an "8"- or "L"- shaped pathway[9),10)] (Fig. 1 (b)). In these studies, it was reported that specimens loaded in two directions showed a greater decrease in strength after reaching the maximum strength than specimens loaded in one direction, and that failure, conjointly, was more severe. However, in those loading methods, the loading pathway up to the aimed point where the deformation angle was at a maximum, as shown in Fig. 1 (a) and (b), involved deformations of the columns that did not exceed the X and Y coordinates of that aimed point. For these reasons, maximum strength was usually recorded for the loading angle at the designated aimed point in many experiments.

Actually, the lateral deformation pattern of a column's top during an actual earthquake is not a straight line, showing a more complex curved behavior. As shown in Fig. 1 (c), the deformation angle in structures during earthquakes reaches a maximum in the 45°direction, but it is thought that there are also curved loading pathway responses that partially exceed the X and Y coordinates of the aimed point. However, there is an extremely small number of experimental examples of this type of displacement pattern.

With this in background, this paper focuses on the bottom of a corner column in the lower stories of high-rise RC buildings. One high-strength SFRC column with concrete strength of f'_c=100N/mm^2 and steel fiber mixing quantity of 1.0 Vol.% was constructed to conduct a structural experiment. A clover-shaped bidirectional lateral load, accompanied by a varying axial loading, were applied at the column's top where the lateral deformation angle reaches a maximum in the 45°direction. This report investigates how the lateral deformation pattern influences the structural performance of the column when the deformation at the top of the column approaches the aimed deformation angle point at 45°. It is worth to mention here that the curve of the loading pattern partially exceeds the X and Y coordinates of the aimed point.

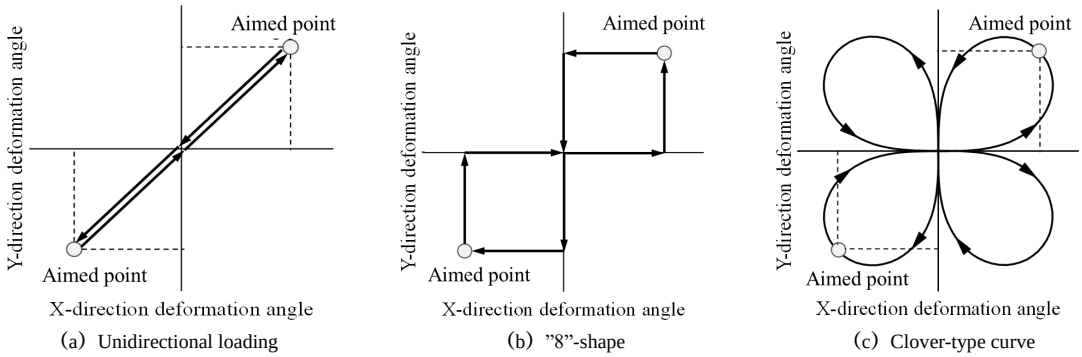

(a) Unidirectional loading (b) "8"-shape (c) Clover-type curve

Fig.1 Lateral deformation pattern

2 Outline of Experimental Research

2.1 Specimen

Characteristics of the specimen are shown in Table 1. Configuration and bar arrangement of the specimen are shown in Fig. 2. The size of the high-strength SFRC column specimen was 1/4th the size of an actual column member. A base plate was set up on the top of the specimen in order to join it with the loading device. The specimen, which was designed to have a flexural failure

mode, had a cross-section of $B \times D$=250×250 mm, and a shear span ratio of 5.00. Assuming a high-rise RC building, the high strength longitudinal bars of the specimen were set as 12-D13 (f_y=685N/mm^2, p_g=2.43%) and its hoops were set as 4-D6@65 (f_y=785N/mm^2, p_w=0.76%). As shown in Photo 2, the steel fibers had a diameter of 0.62 mm, a length of 30 mm, an aspect ratio of 48, a tensile strength over 1,190 N/mm^2, and included hooks on both ends. The steel fiber mixing quantity was set considering a concrete volume ratio of 1.0 Vol.%, which is the mixing quantity that allows an easy casting on-site.

The properties of the concrete and steel material used in the specimen are shown in Tables 2 and 3. Whereas the compressive strength of the concrete was designed so that the target strength during the experiment would be about f'_c=100N/mm^2, at the time of the experiment it reached f'_c=102.8N/mm^2. The specimen was horizontally cast the concrete of the stub was the same as the one of the column.

Table 1 Characteristics of specimen

Specimen	F110-0.33C
Section：$B \times D$	250×250 mm
Length：L	1,250 mm（a/D=5.00）
Longitudinal bars	12-D13（SD685）, p_g=2.43%
Hoops	4-D6@65（SD785）, p_w=0.76%
Steel fiber mixing quantity：V_f	1.0 Vol.% (=80 kg/m^3)

p_g：Reinforcement ratio, p_w：shear reinforced ratio
*1 a/D：shear span ratio
*2 SD□□□, SD：Deformed Steel, □□□：Specified yield strength
Steel bar Cross-sectional Area D13：126.7mm^2, D6：32mm^2

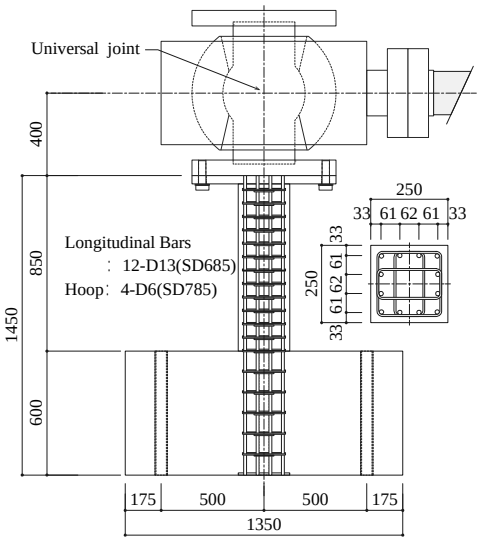

Fig. 2 Configuration and bar arrangement of the specimen

Table 2 Properties of concrete material

f'_c[N/mm^2]	E_c[N/mm^2]	ε_B[×10^{-6}]	σ_{sp}[N/mm^2]
102.8	3.72×10^4	3686	6.37

f'_c：compressive strength, E_c：Young's modulus
ε_B：strain at compressive strength, σ_{sp}：splitting tensile strength

Table 3 Properties of steel material

Type	σ_y [N/mm^2]	E_s [N/mm^2]	σ_u [N/mm^2]	Location of use
D13 (SD685)	698	1.89×10^5	895	Longitudinal bars
D6 (SD785)	920*	1.89×10^5	1061	Hoops

σ_y：yield strength, E_s：Young's modulus, σ_u：tensile strength
*0.2% offset strength

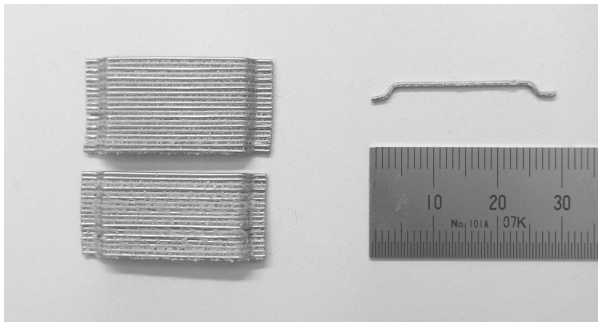

Photo 2 Steel fiber

2.2 Loading and Measurement Methods

The loading system is shown in Photo 3. Experimental loads were applied with a 3-directional loading device. This device has a universal joint system that would be set at the top of the specimen. The universal joint system is connected to horizontal jacks in the X and Y directions and a vertical jack (Z-direction jack). A biaxial pin was also set up at the end of each horizontal jack, and a bidirectional linear slider which allows motions in the X and Y directions was set up on the upper end of the vertical jack. By such arrangement, this loading system can induce displacements of the specimen's top and at any given space location while still introducing a constant axial loading in the vertical

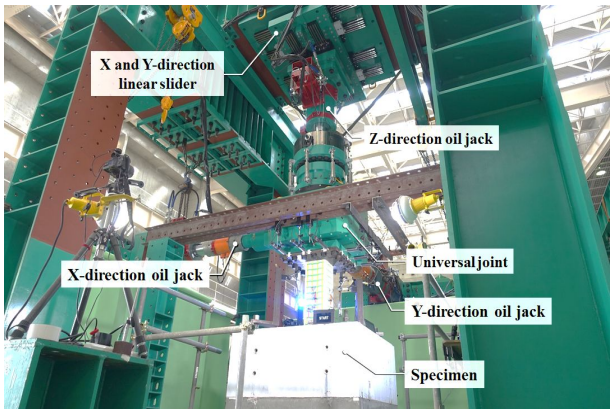

Photo 3 3-directional loading system

direction. During the experiment, the specimen's stub was fixed at a rigid base by prestressing steel bars, after which the base plate of the specimen's top was connected to the universal joint, and a horizontal and vertical forces were applied.

An axial load with a ratio η=0.20 ($\eta=N/BDf'_c$, N：axial load, B：column width, D：depth, f'_c：concrete strength) was applied at the start of the experiment through the vertical jack at the specimen's top, expressing a long-term axial load. In order to more accurately simulate the column member behavior under actual earthquakes, and referring to the study conducted by Pampanin et al.,[11], the strokes of the horizontal jack in the X and Y directions were controlled, and force was applied so that the lateral deformation pattern on the specimen's top would form a clover-shape as shown in Fig. 3 and represented by the function in formula (1). A loading history is shown in Fig. 4. Loading cycles with increasing displacement amplitudes were applied so that the deformation angle R accompanying the horizontal displacement from the origin point and determined in formula (2) would be equal to R=1.0, 2.0, 4.0, (2.0), 5.0, 7.5, (5.0), 10, 15, 20, 30, and 40×10^{-3} rad in the 45 ° direction. The cycle within () was a small cycle considered between larger cycles in order to determine changes of the hysteretic characteristics.

$$(R_x{}^2 + R_y{}^2)^4 - (R_x{}^2 - R_y{}^2)^2 = 0 \quad (1)$$

$$R = \sqrt{R_x{}^2 + R_y{}^2} \quad (2)$$

where, R_x：deformation angle in the X direction ($R_x=\delta_x / L$, δ_x：column's top displacement in the X direction, L：length), R_y：deformation angle in the Y direction ($R_y=\delta_y / L$, δ_y：column's top displacement in the Y direction), and R：spatial deformation angle.

Additionally, a cycle was achieved when the clover-type loading, shown in Fig. 3, traced the 1st to 4th quadrants (1st quadrant: SE quadrant, 2nd quadrant: NE quadrant, 3rd quadrant: NW quadrant, 4th quadrant: SW quadrant). Each loading cycle was conducted twice for each deformation angle (except for $R=40\times10^{-3}$ rad). The lateral load was applied in the following order: SE quadrant (counter-clockwise) → NW quadrant (clockwise) → SW quadrant (clockwise) → NE quadrant (counter-clockwise). The loading order was such that the load amplitudes in the X and Y directions were irregularly positive and negative, as shown by the solid and dotted lines in Fig. 4, respectively.

With regards to the axial loads on the column, this study targeted the corner column's bottom for the lower story of high-rise RC buildings, as shown in Fig. 5. The specimen was planned such that the maximum compressive axial load ratio would be η=0.33 in the SE quadrant, and the maximum tensile axial load $N_t=-0.9a_g \cdot f_y$ in the NW quadrant (a_g：cross-sectional area of longitudinal bars, f_y：yield strength of longitudinal bars), and when applying the axial loads in the SW and NE quadrants, the maximum axial load ratio was planned to be η = 0.20, assuming a behavior of an interior central column. However, as it will be explained in Section 3.1 “Damage progression”, the adhesion between the base plate on the upper end of the specimen and concrete was severed during the $R=7.5\times10^{-3}$ rad loading cycle in the NW quadrant, and a fixed constant tensile axial force could not be applied to the specimen; hence, the target axial load was changed so that the axial load ratio was η=0.10 from the loading cycle $R=10\times10^{-3}$ rad in the NW quadrant. As shown in formula (3), the varying axial loading generated in each of the X and Y directions were applied such that they could be added to the long-term axial load, and they followed the axial load pattern shown in Fig. 6. Half of the target axial loading (η=0.33, 0.10, -0.90) was applied for each of the shear forces in the X and Y directions when they reached the calculated ultimate flexural strength value (New Zealand Standard formula[12]) in the X-axial and Y-axial directions. Therefore, the target axial load was fully loaded when each of the shear forces in the X and Y directions reached the calculated ultimate flexural strength value[12].

$$N = 0.20BDf'_c + f(Q_x) + f(Q_y) \quad (3)$$

where, $f(Q_x)$： varying axial loading due to the shear force in the X direction (Fig. 6 (a)) and $f(Q_y)$：varying axial loading due to the shear force in the Y direction (Fig. 6 (b)). Furthermore, a displacement meter in each of the X and Y directions, which was fixed on the rigid base, was attached to the central part of each of the two sides of the base plates on the specimen's top in order to measure the displacements in the specimen's top in the X and Y directions. An optical full-field three-dimensional displacement / strain measurement system based on digital image correlation[13] was set on the northeastern face of the specimen to measure strains on its northern and eastern faces.

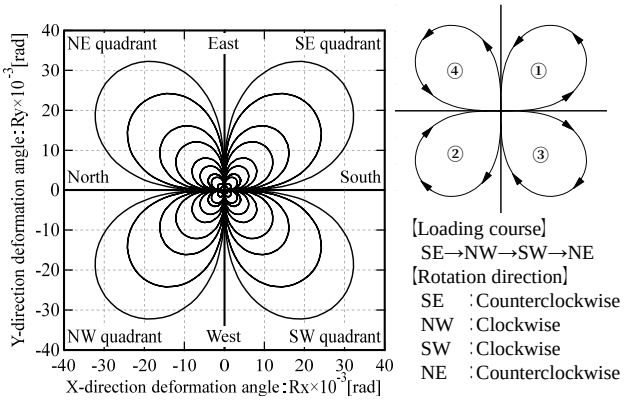

Fig. 3 Lateral deformation pattern at specimen's top

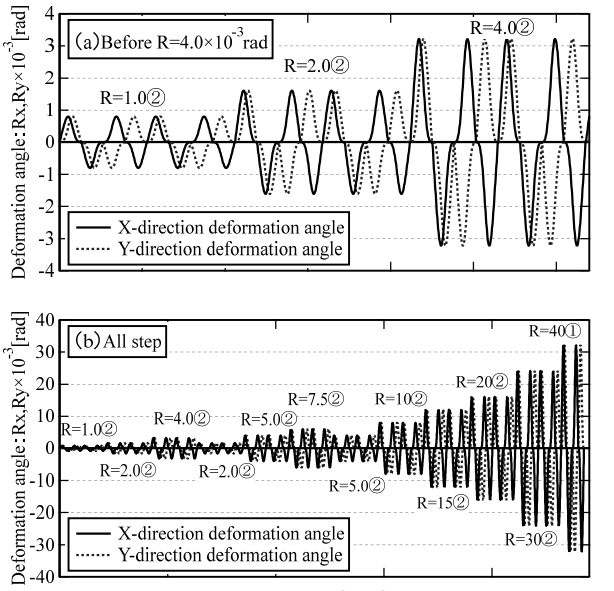

Fig. 4 Loading history

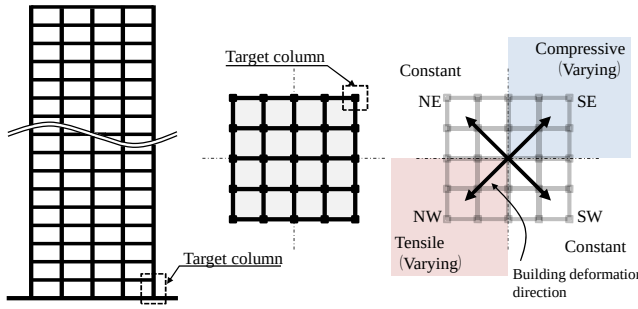

Fig. 5 Basis of axial loading rule

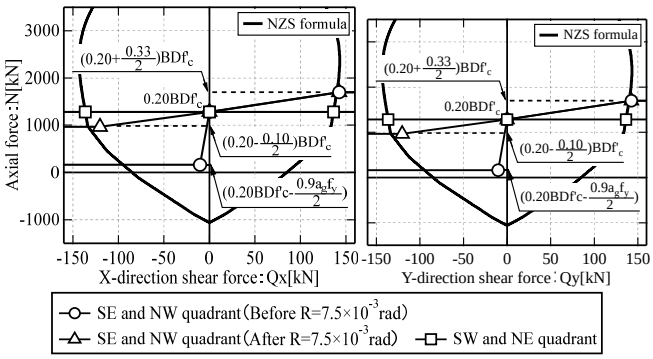

Fig. 6 Axial loading pattern

Table 4 Axial force rule for column

Quadrant	Axial loading ratio	Axial load type
SE	0.20～0.33	Varying axial loading
NW	Before R=10×10^{-3} rad：0.20～-0.90 After R=10×10^{-3} rad：0.20～0.10	Varying axial loading
SW	0.20	Constant axial loading
NE	0.20	Constant axial loading

3 Test Results

3.1 Damage Progression

Damage conditions on the western and southern faces at the end of both the R=15×10^{-3} rad loading cycle and the experiment are shown in Photos 4 and 5, respectively, and the major events that occurred within some loading cycles for each quadrant are shown in Table 5. Damage in each quadrant progressed as follows:

(1) SE quadrant

Flexural cracks were observed on the most tensioned corner during the R=2.0×10^{-3} rad loading cycle in the SE quadrant, while the compressive axial load increased. The increase in the deformation angle resulted in an increased number of flexural cracks and crack widths on the tensile edge. Compressive yielding occurred in the longitudinal bars on the most compressed corner during the R=10×10^{-3} rad loading cycle, and at that time, concrete crushed. Tensile yielding occurred in the longitudinal bars on the most tensioned corner during the R=15×10^{-3} rad loading cycle, and the increase in the deformation angle extended the concrete crushing area along the member axis and toward the section depth directions.

(2) NW quadrant

Flexural cracks were observed on the most tension corner during the R=1.0×10^{-3} rad loading cycle in the NW quadrant, and horizontal cracks formed in intervals of the hoops during the R=2.0×10^{-3} rad loading cycle due to tensile axial loads acting on the specimen. As the adhesion between the base plate on the upper end of the specimen and concrete was severed during the R=7.5×10^{-3} rad loading cycle, tensile axial load could not be applied to the specimen due to the developing gap between the base plate and concrete. So, the loading pattern of the varying axial load was changed so that the axial load ratio would be η=0.10 when each of the shear forces in the X and Y directions acting on the column would reach the ultimate flexural strength (NZS

formula[12]) of the column in both directions from R=10×10^{-3} rad. Compressive yielding then occurred in the longitudinal bars on the most compressed corner during loading cycle R=15×10^{-3} rad, and the concrete crushed during loading cycle R=20×10^{-3} rad. Subsequent increase in the deformation angle extended the concrete crushing area along the member axis and toward the section depth directions, similar to what happened in the SE quadrant.

(3) SW and NE quadrants

Similar behaviors were observed in both the SW and NE quadrants, which were under a constant axial load. Flexural cracks were observed in the most tensioned corner during loading cycle R=4.0×10^{-3} rad, and the increase in the deformation angle resulted in an increase in the number of flexural cracks and widths on the tensile edge. Compressive yielding occurred in the longitudinal bars on the most compressed corner during the R=15×10^{-3} rad loading cycle, and the concrete crushed on the compressed side of the corner. Subsequent increase in the deformation angle extended the concrete crushing area along the member axis and toward the section depth directions, similar to what happened in other quadrants.

Compressive yielding of the most compressed corner and crushing of the concrete were observed in each quadrant, but no spalling of the cover concrete occurred before R=30×10^{-3} rad, and no wide-area spalling of the cover concrete occurred during testing.

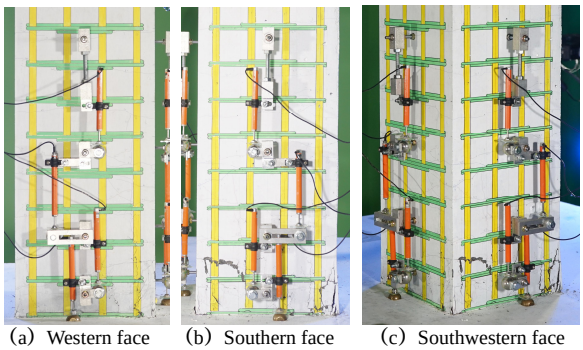

(a) Western face (b) Southern face (c) Southwestern face

Photo 4 Damage of specimen after R=15×10^{-3} rad

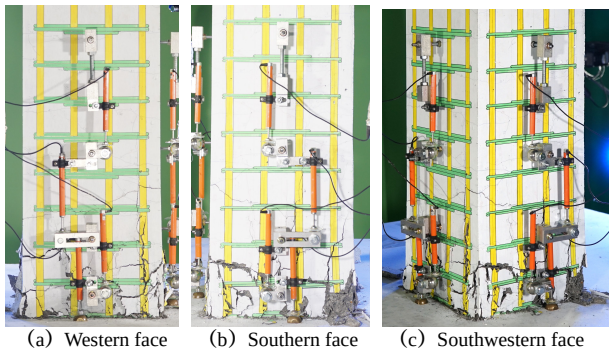

(a) Western face (b) Southern face (c) Southwestern face

Photo 5 Damage of specimen at the test end

Table 5 Major events of each quadrant

R [rad]	SE quadrant (varying axial loading)	NW quadrant (varying axial loading)	SW quadrant (constant axial loading)	NE quadrant (constant axial loading)
1.0×10^{-3}	—	Flexural crack	—	—
2.0×10^{-3}	Flexural crack	—	—	—
4.0×10^{-3}	—	Tensile yielding	Flexural crack	Flexural crack
10×10^{-3}	Concrete crushing Compressive yielding	Axial loading ratio η=-0.90→+0.10	—	—
15×10^{-3}	Tensile yielding	Compressive yielding	Concrete crushing Compressive / Tensile yielding	Concrete crushing Compressive / Tensile yielding
20×10^{-3}	—	Concrete crushing	—	—

3.2 Hysteresis Loop

The shear force-deformation angle relationships for both the X and Y directions are shown in Fig. 7, and the shear force-deformation angle relationships for both the X and Y directions in the SE and NW quadrants, and the SW and NE quadrants are shown in Figs. 8 and 9, respectively. Each figure shows the deformation angle R obtained from formula (2). The shear force at the reach aimed point vicinity gradually began to decrease in the small deformation range on each of the quadrants, the hysteresis loop had a circular trend, and a distinctive shape was observed.

In the SE quadrant, there was little decrease in strength accompanying repeated loads with a deformation angle of less than R=10×10^{-3} rad, at which the concrete crushed, and compressive yielding of the longitudinal bars occurred. Maximum strength was recorded in both the X and Y directions for the subsequent loading cycle of R=15×10^{-3} rad, and a gradual decrease in strength was observed. The shear forces in the X and Y directions in the SE quadrant did not simultaneously reach the ultimate flexural strength values calculated by the NZS formula[12], so the axial load ratio that was loaded at the maximum strength was η=0.27. In the NW quadrant, stiffness rapidly decreased when the tensile axial force was loaded until R=7.5×10^{-3} rad, and strength increased at an almost constant rate. Stiffness increased after R=10×10^{-3} rad when the target axial load ratio value was changed to η=0.10, where a hysteresis loop pattern similar to that in the other quadrants was observed. In the NW quadrant,

strength gradually decreased once the maximum strength was recorded in both the X and Y directions during the R=15×10^{-3} rad loading cycle where compressive yield of the longitudinal bars occurred. The NW quadrant, covering a small axial load ratio, had the smallest decrease of strength. The axial load ratio reached during the maximum strength was η=0.13 in the NW quadrant, since the shear forces in the X and Y directions did not reach the ultimate flexural strength values calculated by the NZS formula[12] simultaneously.

Similar behaviors were observed in both the SW and NE quadrants, where the axial force was constant, and there was little decrease in strength accompanying repeated loads with a deformation angle of less than R=15×10^{-3} rad, at which the concrete crushed and compressive yielding of the longitudinal bars occurred. Maximum strength was observed in both the X and Y directions for the subsequent loading cycle of R=15×10^{-3} rad, after which a gradual decrease in strength was observed.

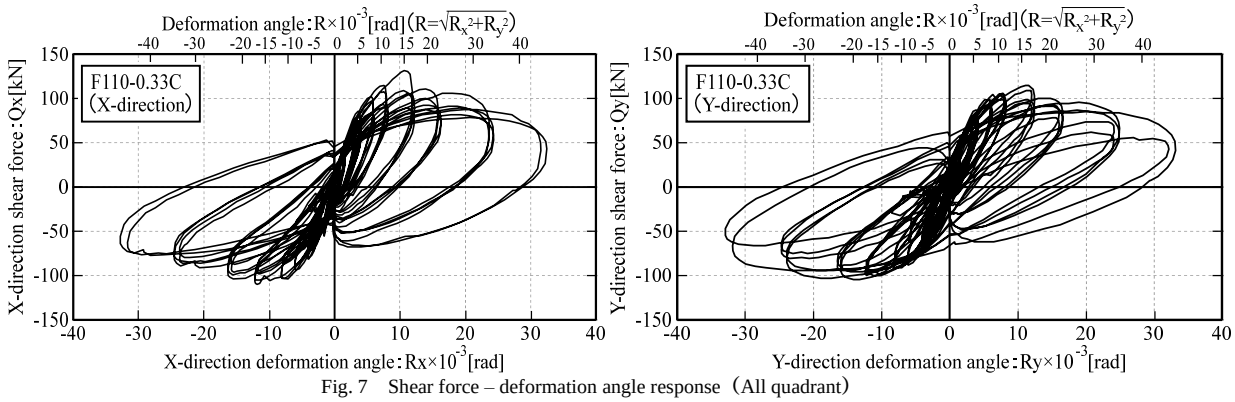

Fig. 7 Shear force – deformation angle response (All quadrant)

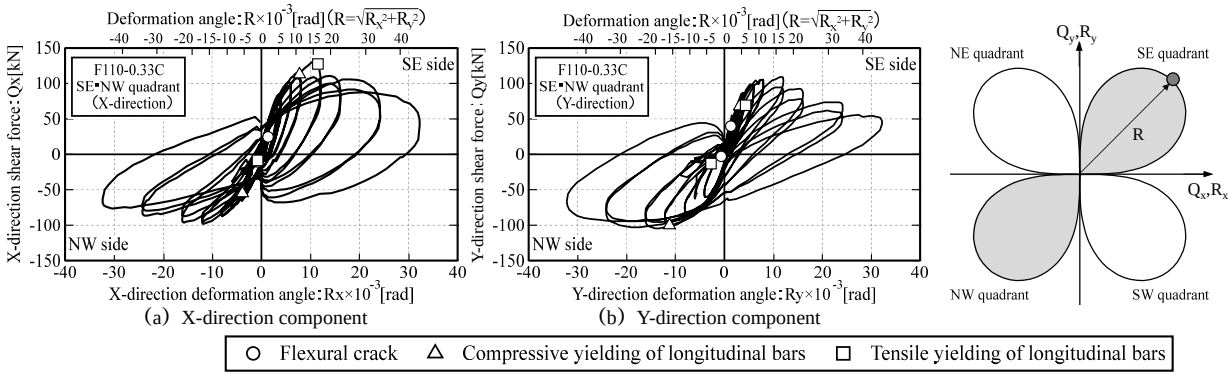

Fig. 8 Shear force – deformation angle response and major events (SE and NW quadrant)

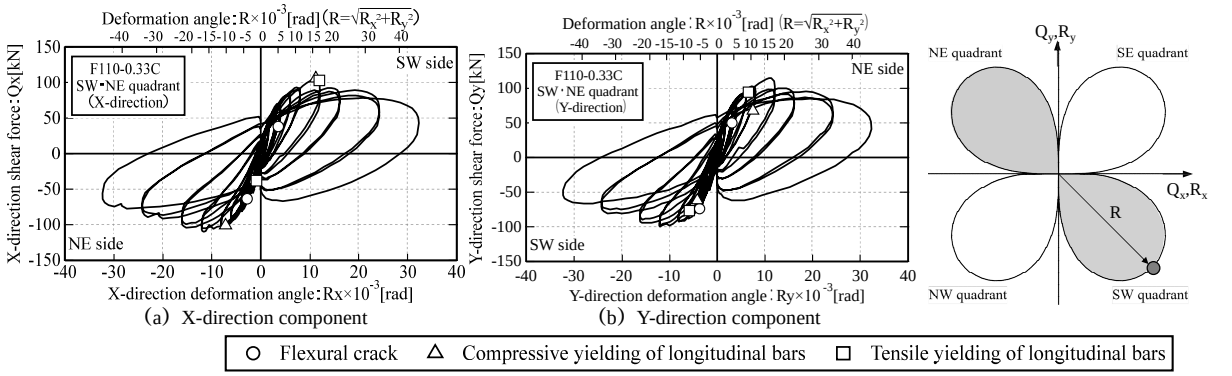

Fig. 9 Shear force – deformation angle response and major events (SW and NE quadrant)

3.3 Stress of Longitudinal Bars

Fig.10 shows the relationships of the axial stress to the deformation angle in the corner longitudinal bars at the peak (45°direction) for each quadrant. The strain of longitudinal bars were measured using strain gages (see Fig. 11 for reference) set up at the critical section of the corner longitudinal bars in the SE quadrant (Gage No. C44) and NW quadrant (Gage No. C11). A bilinear stress-strain pattern was assumed for the longitudinal bars, and stresses were calculated using the measured values obtained from the strain gages. In SE quadrant and NW quadrant, the stresses of the longitudinal bars increased at the locations of

the gage No.C11 and C44. Compressive and tensile yielding occurred at R=10～15×10^{-3} rad. Up to R=7.5×10^{-3} rad., a compressive stress of approximately σ=-100 N/mm^2 was present in the SW and NE quadrants, where the Gage No. C11 and C44 horizontal locations were in the vicinity of the neutral axis. Thus, the neutral axis was assumed to be orthogonal to the 45° direction of the applied deformation angle, since the stresses that developed at C11 and C44 were similar. Meanwhile, there were differences in the stresses between C11 and C44 at and beyond R=10×10^{-3} rad, where the concrete began first to crush: stresses increased on the tensile side in C11 and on the compressive side in C44, and the neutral axis was at an incline from 45°, after the deformation angle R=10×10^{-3} rad where the concrete crushing occurred. It is thought that the lateral deformation pattern influenced the stress level of longitudinal bars at the peak, since tensile stresses developed first at C11, and compressive stresses developed first at C44 during the SW and NE quadrants loading.

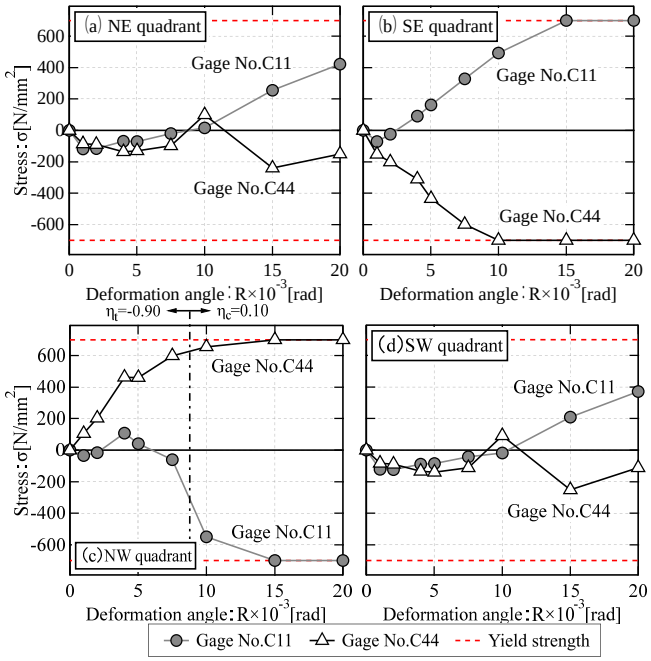

Fig. 10 Longitudinal bar stress – deformation relationships

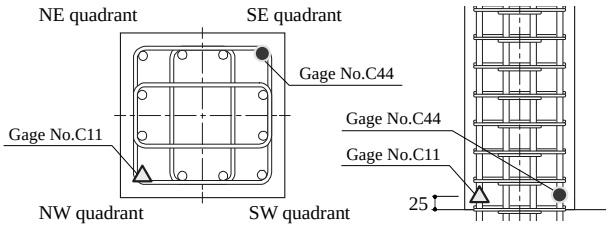

Fig. 11 Strain gage location

3.4 Maximum and Minimum Principal Strain

Fig.12 shows the maximum principal strain distributions on the northern and eastern faces of the specimen at R=15×10^{-3} rad in each quadrant. The maximum principal strains were measured using digital image correlation on the northeastern side of the specimen. It was observed that the strains on the most tension corner, tend to increase in each quadrant, and the maximum principal strain distributions followed cracks' locations. Also, it was observed that the areas where a maximum principal strain value over 1.0% was measured were at about 2.0D (D: column depth) from the critical section in the SE quadrant, where the axial load ratio was η=0.27, 2.5D in the SW quadrant, where the axial load ratio was η=0.20, and 3.0D in the NW quadrant, where the axial load ratio was η=0.13. Thus, a lower location of the area of the maximum principal strain distribution was observed as the axial loading ratio increased.

Fig. 13 shows the minimum principal strain distributions on the northern and eastern faces of the specimen at R=15×10^{-3} rad in each quadrant. The minimum principal strains were measured using digital image correlation on the northeastern side of the specimen. The arrows in the figure indicate the direction and magnitude of the minimal principal strains. It was observed that the measured areas where compressive strains exceeded 0.2% tended to become narrower when the locations of these areas were farther from the critical section. Furthermore, the area tended to expand further toward the most tensioned corner as the axial load ratio increased. As the strains in the all corners included large measurement errors, their values can be used only for reference.

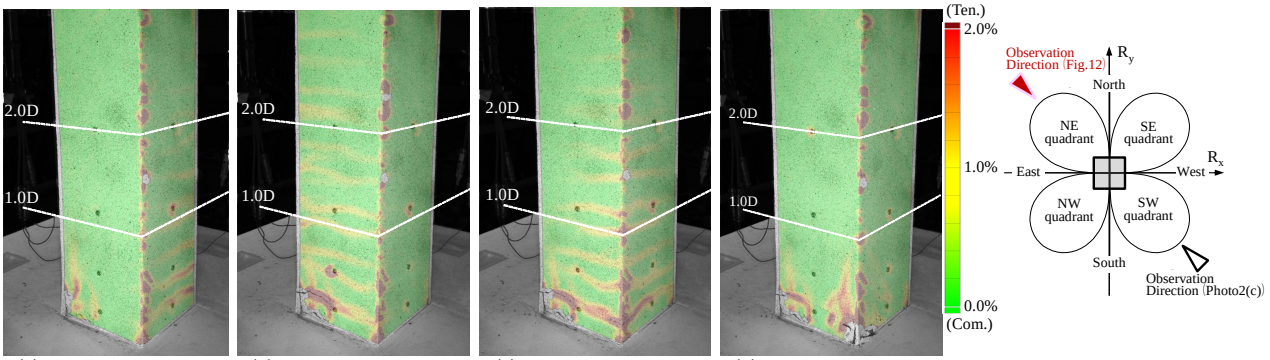

(a) SE direction loading (b) NW direction loading (c) SW direction loading (d) NE direction loading

Fig. 12 Distribution of maximum principal strain on the North and East side (R=15×10^{-3} rad)

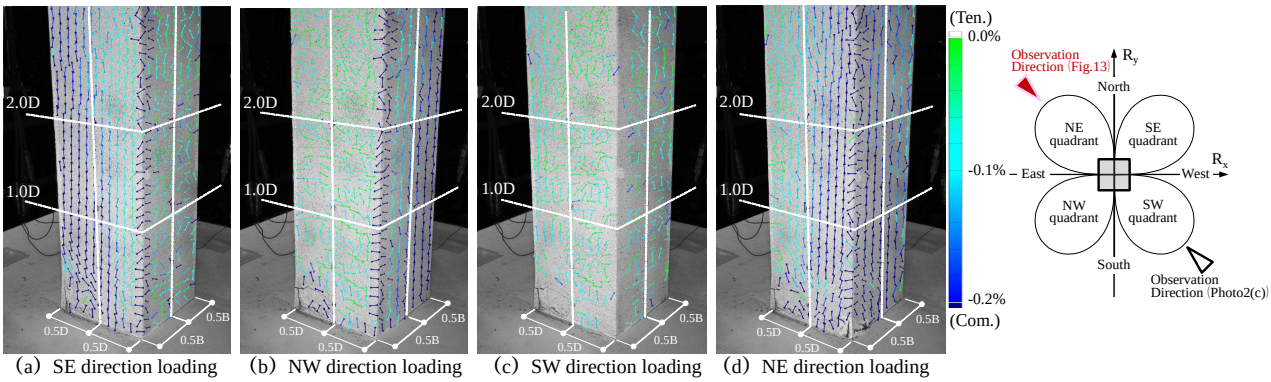

(a) SE direction loading (b) NW direction loading (c) SW direction loading (d) NE direction loading

Fig. 13 Distribution of minimum principal strain on the North and East side (R=15×10^{-3} rad)

4 Seismic Performance Analysis

4.1 Maximum Strength and 45°Direction Strength

Fig.14 shows the shear force-deformation angle relationship of the specimen. In this section, the total shear force acting on the specimen was calculated as the sum of the X- and Y-direction component vectors of the shear forces acting in the X and Y directions of the specimen based on formula (4), in order to analyze the relationship between the maximum strength and the calculated ultimate flexural strength of the specimen.

$$Q = \sqrt{{Q_x}^2 + {Q_y}^2} \qquad (4)$$

where, Q：shear force, Q_x：shear force in the X direction, and Q_y：shear force in the Y direction.

Also, Fig.14 shows the points of maximum strength (Q_{max}) resulting from the component vectors of the shear forces, maximum shear force in the 45° direction ($Q_{max,45}$), and the 80% of the maximum strength defined by the limit deformation angle (R_{80}). Furthermore, the ultimate flexural strength values (Q_{cal}) calculated in the X- and Y directions considering the axial load ratios in each quadrant are indicated in Fig. 14. The ultimate flexural strength value was calculated based on the NZS formula[12)]

and ACI stress block method[14)]. The later method evaluated the strength values with higher accuracy. The effects of the steel fibers were not considered in the both calculations.

From Fig. 14, the maximum shear strength was recorded at a deformation angle R=12～19×10^{-3} rad and the increase of the axial load ratios resulted in smaller deformation angles at the occurring time of the maximum strength. In the three quadrants (excluding the SW one), the maximum strength exceeded the calculated ultimate flexural strength value in the 0° direction, which was based on the ACI stress block method[14)], and the recorded values in the SW quadrant were nearly identical to the calculated values.

Fig.15 and Table 6 show comparisons between experimental values after making corrections relative to the P-Δ effect and the calculated ultimate flexural strength values. Fig. 15 shows the yield surface for the bidirectional bending. The yield surface expressed by the formula (5) with the coefficient α = 2.0, and a linear yield surface based on Ferguson's proposal[7)] are shown in the figure. For the both yield surfaces, the calculated ultimate flexural strength values in the X and Y directions were calculated

using the ACI stress block method[14].

$$(Q_x/Q_{ux})^{\alpha} + (Q_y/Q_{uy})^{\alpha} = 1.0 \qquad (5)$$

where, Q_{ux}：ultimate flexural strength in the X direction, and Q_{uy}：ultimate flexural strength in the Y direction.

As shown in Fig. 15 and Table 6, the maximum strength of the specimen was recorded at a loading angle θ=20～30°, and was 1.18～1.36 times the value calculated using the linear equation of Ferguson's proposal[7] for the loading angle at the time of maximum strength. As shown by the loading angle in Fig. 16, this paper defines the origin prior to the loading of each quadrant at θ=0°, and the origin after the loading of each quadrant at θ=90°, with θ ranging from 0～90° for each quadrant.

The maximum shear force in the loading direction θ=45° was recorded prior to the maximum strength in the NE and NW quadrants, and after the maximum strength in the SE and SW quadrants. As shown in Fig. 15 and Table 6, the maximum shear force of the specimen in the 45° direction was 1.04～1.18 times the value calculated using the linear equation of Ferguson's proposal[7], and showed a decreasing safety factor tendency relative to the maximum strength time. Furthermore, as seen in Table6, the maximum shear force at the loading angle θ=45° was 0.80～0.97 times the maximum strength of the specimen and the increase of the axial load ratios resulted in a decrease of the maximum shear force ratios at θ=45° for the maximum strength.

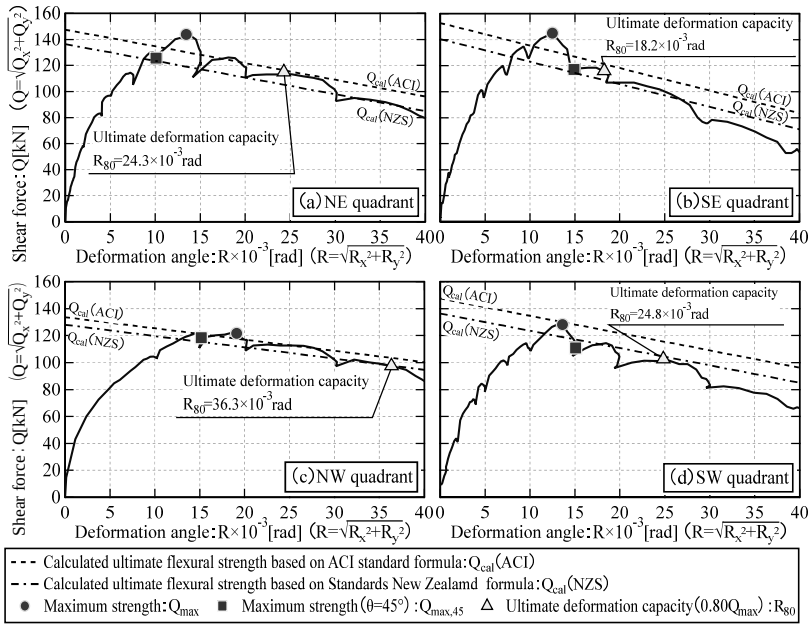

Fig. 14 Shear force – deformation angle response

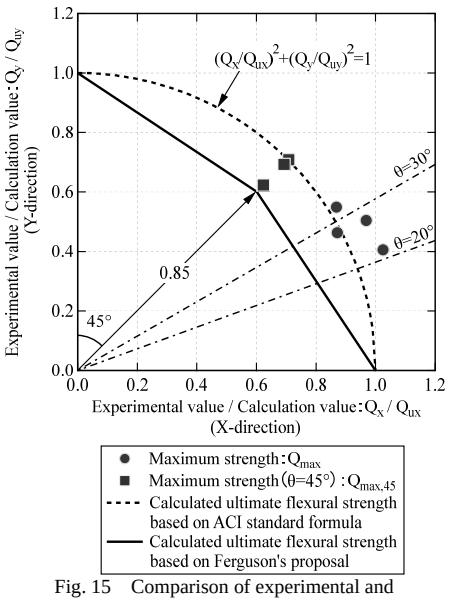

Fig. 15 Comparison of experimental and calculated values

Table 6 Ultimate flexural strength（calculation and experimental values）

Loading direction	Experimental value*1			Calculated value		Q_{max} / Q_{cal}	$Q_{max,45}$ / $Q_{cal,45}$
	Q_{max}[kN]	$Q_{max,45}$[kN]	$Q_{max,45}$ / Q_{max}	Q_{cal}*2[kN]	$Q_{cal,45}$*2[kN]		
SE	168.5（R=12.5×10⁻³rad）	134.5（R=14.9×10⁻³rad）	0.80	130.1	129.9	1.30	1.04
NW	137.3（R=19.1×10⁻³rad）	133.7（R=15.2×10⁻³rad）	0.97	101.3	113.6	1.36	1.18
SW	145.6（R=13.6×10⁻³rad）	130.1（R=15.1×10⁻³rad）	0.89	123.5	125.4	1.18	1.04
NE	161.1（R=13.5×10⁻³rad）	144.5（R=10.1×10⁻³rad）	0.90	123.6	125.4	1.30	1.15

*1 Experimental values which considered the P–⊿ effect

*2 Calculated ultimate flexural strength values based on ACI stress block method[14] and Ferguson's proposed equation[7]

4.2 Loading Angle on Maximum Shear Force

Loading angle transitions when the maximum shear force was recorded in each loading cycle are shown in Fig. 17 for each quadrant. The loading angles of each quadrant are defined in Fig. 16.

For the R=1.0×10⁻³ rad loading cycle, the loading angle at the maximum shear force in the SE quadrant (corresponding to the first horizontal load applied to the specimen) was θ=40.5°, and was slightly smaller than the θ=45° where an elastic body exhibits its maximum strength. The loading angle in the NW quadrant, where the axial load decreased, was θ=62.3° when the maximum shear force was exhibited, and its value was the highest relative to those in other quadrants. The loading angle in the subsequent SW quadrant was θ=24.8° when the maximum shear force was exhibited at R=1.0×10⁻³ rad, and had the smallest value relative to

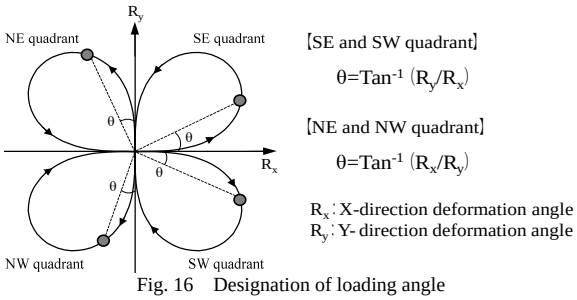

Fig. 16 Designation of loading angle

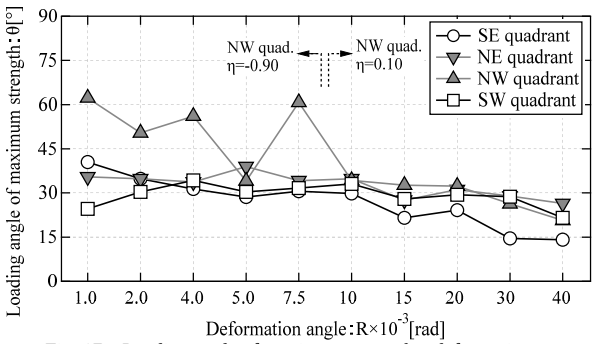

Fig. 17 Loading angle of maximum strength – deformation angle relationship

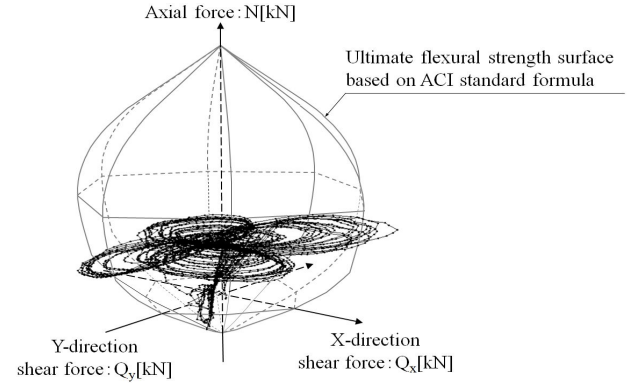

Fig. 18 Comparison of experimental values and ultimate strength surface

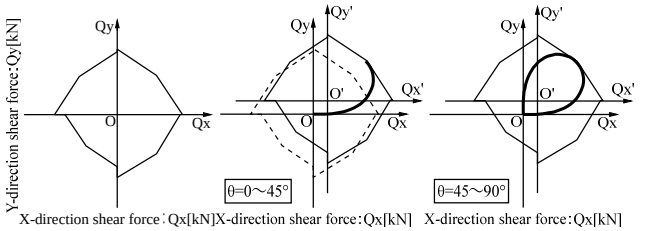

(a) Elastic region (b) Plastic region (θ=0-45°) (c) Plastic region (θ=45-90°)

Fig. 19 Ultimate strength surface movement

those in the other quadrants. Finally, the loading angle in the NE quadrant was θ=35.5°. Subsequently, the loading angle at the time of maximum shear stress from R=2.0×10^{-3} rad (when flexural cracks occurred) was around θ=30° in the SE quadrant where the compressive axial forces increased, and the loading angle tended to decrease from R=10×10^{-3} rad (when concrete crush was observed). The loading angle on the maximum shear force in the NW quadrant, where tensile axial loads were applied, was also around θ=50～60°. The loading angle at the maximum shear force from R=10×10^{-3} rad, where the axial load force was changed to η=0.10, was around θ=30°, similarly to the trends seen in other quadrants. The loading angle showed a decreasing tendency from R=20×10^{-3} rad, where concrete crush was observed.

The loading angle on the maximum shear force in the SW and NE quadrants, where constant axial loads were applied, was also around θ=30°, and the loading angle showed a decreasing tendency from R=15×10^{-3} rad, where concrete crush was observed. Based on the above observations , changing the lateral deformation pattern in the column head to a clover-type pattern resulted in a loading angle at maximum shear force which changed from a small deformation angle, and a loading angle at maximum strength of the column under compressive axial load of around θ=30°. These above-mentioned behaviors were thought to be influenced by the kinematic hardening of the yield surface accompanying the bidirectional bending, and the reasons are explained below.

The relationship between Q_x – Q_y, which represent the shear forces in the X and Y directions, and the acting axial load is shown in Fig. 18. Varying axial loads act on the SE and NW quadrants in this experiment; hence, the specimen behaves within a three-dimensional yield surface as shown in Fig. 18, and thus exhibited an extremely complex behavior. It should be noted that the study explains this behavior by projecting this three-dimensional behavior into a two-dimensional scheme, as shown in Fig. 19. The yield surface was assumed to move in a rigid manner through the stress space following the plastic deformation of the column, according to the kinematic hardening outlined by Prager.[15] As shown in Fig. 19 (a), the restoring force did not reach the yield surface when the specimen was within the elastic domain, so the Q_x - Q_y coordinate system did not move. Subsequently, as shown in Fig. 19 (b), the yield surface moved in a stiff manner when the restoring force reached the yield surface due to an increase in the shear force during loading in the SE quadrant, so the Q_x - Q_y coordinate system moved. Furthermore, as shown in Fig. 19 (c), the Q_x - Q_y coordinate system did not move even when the specimen displacement moved to the origin, so the shear forces in the X and Y directions acting on the specimen at the origin were dragged into the loading quadrant and diagonal side quadrant. This phenomenon occurred in all quadrants and not just in the SE quadrant, so the shear force at the origin in each quadrant was dragged into the quadrant on its diagonal side. A crack surface that was separate from the yield surface was present when the above-mentioned phenomenon occurred in the RC member. Therefore, the phenomenon in which the shear force was

dragged had occurred since the small deformation period.

The Q_x - Q_y relationships at the loading cycles R=1.0, 15 and 30×10^{-3} rad is shown in Fig. 20. The force values when the loading angles were θ=30°, 45°, and 90° are shown in Fig. 20 for each quadrant. In Fig. 20, the cracking surface, which was calculated by multiplying the section modulus in the 0° and 45° directions with the crack strength based on RC standards[16], and linear yield surface based on Ferguson's proposal[7], which used the calculated ultimate flexural strength value in the ACI stress block method[14] are shown. As shown in Fig. 20 (a), the shear forces at the origin (θ=90°) at the end of each quadrant had a tendency to be dragged into the quadrant on the diagonal side. No flexural cracks could be visually confirmed at R=1.0×10^{-3} rad with the exception of the NW quadrant. Although the phenomenon where the shear force was dragged should not occur in what was thought to be an elastic domain; it probably occurred due to nonlinear phenomena that accompany local hair cracks that occurred within the column.

Afterwards, the shear force in each direction reached the yield surface of the calculated ultimate flexural strength value at R=15×10^{-3} rad, and it was confirmed that the shear force was dragged to the quadrant on the diagonal side when the column head displacement returned to the origin. Also, as seen in Fig. 20 (c), the phenomenon in which the shear force was dragged to the origin became greater during larger displacement periods, and the Q_x - Q_y relationship tended to become ever flatter. Next, when focusing on the direction in which the load was initiated in each quadrant (SE, SW quadrants: X direction, NE, NW quadrants: Y direction) for the clover-type column head lateral loading pattern used in this experiment, the displacement amount of that direction exceeded the maximum displacement amount at the loading angle θ=45°, and showed a decreasing pattern. For that reason, when the shear force of either the X or Y direction first reached its maximum at the yield surface, it began to decrease. Furthermore, as shown in Fig. 19, the Q_x - Q_y relationship had already moved when the shear force began to decrease, so the decreased value of the shear force seem larger. As this study adopted a clover-type curve, expressed by formula (1), when the displacement amount in the direction where the load was initiated was at a maximum, the loading angle was θ=31.1°. When once again focusing on Fig. 20 (b) with this in mind, it can be reasoned that the fluctuations in the direction where the load was initiated were relatively larger before θ=31.1° with regards to the loading angles after θ=31.1°, where the displacement amount in that direction was at a maximum for each quadrant. For these reasons, it can be reasoned that the shear force acting on the specimen had a tendency to exhibit its maximum strength at around θ=31.1° in each cycle because the decrease in value of the shear force in the direction where the load was initiated became larger from the loading angle θ=31.1° onwards.

From the above, it can be confirmed that the loading angle at the time of maximum shear force in the column undergoing bidirectional bending where the deformation angle is at a maximum in the 45 ° direction is not always 45°, but instead, is at an approximate angle value in the planar displacement pattern of the RC column where the first displacement decreases in the load direction.

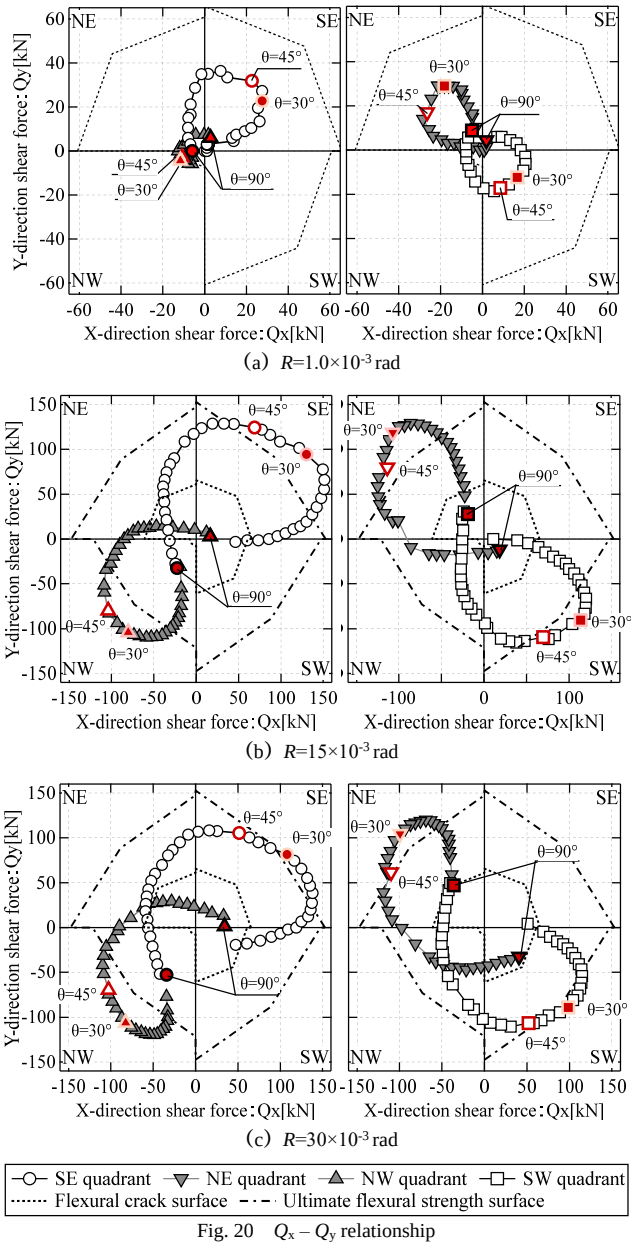

Fig. 20 Q_x – Q_y relationship

5 Conclusions

This study conducted a structural experiment on a flexural yield failure-type specimen, a high-strength SFRC column undergoing a clover-type bidirectional bending where the deformation angle was at a maximum of 45 ° for the lateral deformation pattern of the column's top with varying axial loading. The following results were obtained.

1) Crushing of the cover concrete was prevented up to R=30×10^{-3} rad by mixing steel fiber into the concrete.
2) The loading angle on the maximum strength of the RC column which underwent bidirectional bending was determined based on the displacement in the direction when the load was initiated began to decrease, due to the influence of kinematic hardening of the yield surface.
3) The maximum strength of the specimen was 1.18～1.36 times greater than the ultimate flexural strength value calculated by the linear graphs which used the ACI stress block method[14] and Ferguson's proposal[7]. The values were appropriately evaluated.
4) The 45° direction strength of the specimen was 0.80～0.97 times that of the maximum strength, and 1.04～1.18 times that of the ultimate flexural strength value calculated by the linear graphs which used the ACI stress block method[14] and the Ferguson's proposal[7]. The values were an appropriately evaluated.

The above-mentioned findings were obtained from the experimental data of a single specimen used in this study and thus are based on an extremely small sample size; therefore, these results are within a limited experimental scope. Furthermore, the strength evaluations do not reflect the effects of the steel fibers in the SFRC columns. For this reason, future work is needed to focus on the seismic performance which takes into account the deformation performance of RC columns, including high-strength SFRC columns, which undergo bidirectional bending under clover-type planar deformation pattern.

References

1) JDC Technology Center：Integrated Technology Development Project "H.5.3 Research Report: Development of light-weight / high-rise technologies for RC concrete buildings," Mar. 1993（in Japanese）
2) Ishikawa, Y., Kimura, H., Sawamura, M., Ueda, T.：Performance of high-strength concrete columns using high-strength main bars under combined high axial load and bending moment, Proceedings of the Japanese Concrete Institute, Vol.22, No.3, pp. 943-948, Jun. 2000（in Japanese）
3) Ueda, T., Abe, H., Yamashita, S., Ohtsu, K.：Design and construction of high-rise R/C apartment building of 59 stories, Concrete Journal, Vol. 45, No.3, pp. 39-44, Mar. 2007（in Japanese）
4) Kimura, H., Ishikawa, Y.：Cyclic loading test on RC columns using fiber reinforced high strength concrete, Proceedings of the Japanese Concrete Institute, Vol. 23, No.3, pp. 211-216, Jun. 2001（in Japanase）
5) Y.Ishikawa, H.Kimura, H.Takatsu and H.Ousalem：ULTIMATE DEFORMATION OF R/C COLUMNS USING HIGH-STRENGTH CONCRETE AND HIGH-STRENGTH STEEL BARS UNDER EARTHQUAKE LOADING, 8th International Symposium on Utilization of High-Strength and High-Performance Concrete, pp. 974-981, Oct. 2008
6) Ishikawa, Y., Ogura, F., Aso, N., Kake, S., Ohta, Y.：Experimental study on flexural performance of high strength steel fiber reinforced concrete columns under axial and lateral loadings. Part 1: Outline of experiment and damage progress, Summaries of Technical Papers of Annual Meeting, Architectural Institute of Japan, Vol. 25, StructureⅣ, pp. 305-306, Sep. 2018（in Japanese）
7) Phil Moss Ferguson：Reinforced Concrete Fundamentals, 4th edition, Wiley, 1958
8) Okada, T., Seki, M., Asai, S., Okada, T.：Restoring force of RC concrete columns undergoing fixed axial load and repeated bidirectional bending / shearing force (part 1: experimental methods), Summaries of Technical Papers of Annual Meeting, Architectural Institute of Japan, Vol. 51, pp. 1447-1448, Aug. 1976（in Japanese）
9) Li, K.-N., Otani, S., Aoyama, H.：Behavior of R/C columns under varying axial and earthquake loads, Conference Proceedings of the Japanese Concrete Institute, Vol.8, pp. 489-492, 1986（in Japanese）
10) Uehara, H., Minami, K.：Elasto-plastic behavior of reinforced concrete columns under biaxial flexure and shear reversals, Conference Proceedings of the Japanese Concrete Institute, Vol.11, No.2, pp. 223-228, 1989（in Japanse）
11) S.Pampanin, U.Akguzel and G.Attanasi：SEISMIC UPGRADING OF 3-D EXTERIOR R.C. BEAM COLUMN JOINTS

SUBJECTED TO BI-DIRECTIONAL CYCLE LOADING USING GFRP COMPOSITES，8th International Symposium on Fiber Reinforced Polymer Reinforcement for Concrete Structures, Patras, Greece Jul. 2007

12） Standards New Zealand：Concrete Structures Standard Part 1-The Design of Concrete Structures，Part 2-Commentary on The Design of Concrete Structures，1995

13） Kawasaki, Y.：The process of validation for simulation models using optical 3D measurement techniques by DIC, and case studies，Proceedings on the Conference on Computational Engineering and Science，Vol.18，Jun. 2013（in Japanese）

14） American Concrete Institute：Building Code and Commentary ACI 318-95/318R-95，1995

15） W.Prager，”A New Method of Analyzing Stresses and Strains in Work-Hardening Plastic Solid”，Journal of Applied Mechanics，ASME，Vol. 23，pp. 493-496，1956

16） Architectural Institute of Japan：Standard for structural calculation of steel reinforced concrete structures，2018